

Towards Image Guided Magnetic Resonance Elastography via Active Driver Positioning Robot

Waiman Meinhold , Efe Ozkaya , Derek Petti , Vaughn Rice, Emily Triolo , Fargol Rezayaraghi, Paul Kennedy, Lazar Fleysher, Ai-Ping Hu, Jun Ueda , Senior Member, IEEE, and Mehmet Kurt 

Abstract—Magnetic Resonance Elastography (MRE) is a developing imaging technique that enables non-invasive estimation of tissue mechanical properties through the combination of induced mechanical displacements in the tissue and Magnetic Resonance Imaging (MRI). The mechanical drivers necessary to produce shear waves in the tissue have been a focus of engineering effort in the development and refinement of MRE. The potential targeting of smaller and stiffer tissues calls for increases in actuation frequency and refinement of mechanical driver positioning. Furthermore, the anisotropic nature of soft tissues results in driver position related changes in observed displacement wave patterns. These challenges motivate the investigation and development of the concept of active MRE driver positioning through visual servoing under MR imaging. **Objective:** This work demonstrates the initial prototype of an MRE driver positioning system, allowing capture of displacement wave patterns from various mechanical vibration loading angles under different vibration frequencies through MR imaging. **Methods:** Three different configurations of the MRE driver positioning robot are tested with an intervertebral disc (IVD) shaped gel phantom. **Results:** Both the octahedral shear stress signal to noise ratio (OSS-SNR) and estimated stiffness show statistically significant dependence on driver configuration in each of the three phantom IVD regions. **Conclusion:** This dependence demonstrates that driver configuration is a critical factor in MRE, and that the developed robot is capable of producing a range of configurations. **Significance:** This work presents the first demonstration of an active, imaging guided MRE driver positioning system, with significance for the future application of MRE to a wider range of human tissues.

Index Terms—Magnetic resonance elastography, magnetic resonance imaging, piezo actuator, image guided robotics.

I. INTRODUCTION

DEGENERATIVE Disc Disease (DDD) is a common musculoskeletal disorder, which usually leads to pain syndromes and mechanical spine dysfunction [1]. Early detection or prognosis of disc degeneration is critical to symptom management. However, this has been extremely challenging due to limited success in finding *in vivo* imaging biomarkers for the stage of degeneration. Although several imaging-based markers such as the morphology and brightness of the disc in a T2-weighted magnetic resonance (MR) image have been previously proposed, they demonstrated limited correlation with the stage of the disc degeneration [2]–[6]. An ideal imaging parameter would be the elasticity of the disc, which directly correlates with the underlying pathology. Therefore, there is a significant need to develop and find such imaging-based *in vivo* biomarkers that can be used for the assessment of intervertebral disc degeneration.

Thanks to the advancements in MR imaging, MR Elastography (MRE) has emerged as a non-invasive tool which makes it possible to probe biological tissues *in vivo* and measure their mechanical properties [7]. For MRE imaging of small tissues such as the intervertebral disc (IVD), targeted harmonic loading is required so as to maximize the signal-to-noise ratio (SNR) [8], [9]. Moreover, propagating shear wavelength should not surpass the size of the region of interest (ROI). In other words, the shorter the wavelength the more sensitive the displacement data will be to local stiffness variations within an imaging target.

Although increased actuation frequency allows placement of shorter shear waves within a targeted ROI, it creates challenges due to attenuation. This situation led to the investigation of multi-driver units [10]–[13]. With multi-driver units, it is aimed to increase the survivability of propagating shear waves by benefiting from constructive wave interference [12]. In order to achieve a location specific constructive wave interference, control of MRE driver positioning is needed compared to the studies in which MRE driver positioning/placement is done manually [14].

Since medical robots are becoming an essential part of the clinician's arsenal for biopsy, diagnosis, therapy, and prognosis [15]–[20], precise robot control in clinical settings is especially crucial for the success of the targeted outcome. Major challenges during closed loop control of robotic systems are:

Manuscript received 4 January 2022; revised 14 March 2022; accepted 6 April 2022. Date of publication 19 April 2022; date of current version 20 October 2022. This work was supported by Peer-Reviewed Medical Research Program Discovery Award from Congressionally Directed Medical Research Program, U.S. Army, under Award W81XWH-20-1-0043. (*Corresponding author:* Waiman Meinhold.)

Jun Ueda is with the Woodruff School of Mechanical Engineering, Georgia Institute of Technology, USA.

Waiman Meinhold is with the Woodruff school of Mechanical Engineering, Georgia Institute of Technology, Atlanta, GA 30332 USA (e-mail: wmeinholt@gatech.edu).

Efe Ozkaya, Paul Kennedy, and Lazar Fleysher are with the BioMedical Engineering and Imaging Institute, Icahn School of Medicine Mount Sinai, USA.

Derek Petti and Vaughn Rice are with the Department of Mechanical Engineering, Stevens Institute of Technology, USA.

Emily Triolo, Fargol Rezayaraghi, and Mehmet Kurt are with the Department of Mechanical Engineering, University of Washington, USA.

Ai-Ping Hu is with the Intelligent Sustainable Technologies Division, Georgia Tech Research Institute, USA.

Digital Object Identifier 10.1109/TBME.2022.3168494

use of expensive or fragile sensory equipment for feedback, and latency in the remote system [21]. These challenges can be overcome by the use of visual servoing [22]. In visual servoing, simultaneous detection and tracking of the surgical instrument/robotic manipulator with the targeted tissue/body area inside the field of view can be performed. As expected, the quality of acquired images for visual servoing are affected by the imaging device. This device can be an external camera, microscope, or an endoscope. In addition to these devices that contain optical lenses, medical imaging modalities such as MRI, computed tomography (CT), ultrasound (US), X-ray fluoroscopy, or endoscopic imaging can be used [23]. Among these modalities, MRI surpasses the others by having better soft tissue contrast, volumetric imaging capability, high spatial resolution, and high sensitivity for detecting small regions [24].

This work details the design and evaluation of a 5 °-of-freedom (DOF) active MRE driver positioning system for image guided MRE that is targeted to be used for the non-invasive assessment of disc degeneration in the lumbar region, *in vivo*. Application of MRE imaging to identifying the degeneration level of the intervertebral disc (IVD) has already been performed by a few research groups mostly on excised IVD tissue [25]–[27]. However, to the authors' knowledge, during MRE of a small imaging target, no study has used the MRI scanner as a feedback device through visual output to control the MRE driver's position.

For MRE driver positioning, the system reported here utilizes hydraulic actuators which do not create any electromagnetic interference while being placed inside the MRI bore and as the MRE driver vibration source it uses a strain amplified piezoelectric driver (APA150M-NM, Cedrat Technologies) to produce shear waves within the imaging target.

The robot's configuration measurement is achieved by injecting an MR contrasting fluid (water) inside the cavities of the 5-DOF system components. In other words, the components which contain water become visible under MR imaging. For initial MRE experiments, a tissue-mimicking phantom that replicated IVD geometry was used. The system proposed in this work, which requires the combination of positioning control with MRE actuation, is shown in Fig. 1.

This work is presented as follows. First, the mechanical design and kinematics of the 5-DOF MRE driver positioning robot are presented. Potential control methods are described, with the MRE specific configuration requirements indicating a sequential planar and 5th axis control scheme. Finally, a remotely operated version of the robot is manually placed in 3 different configurations to investigate the effect of MRE driver orientation on both displacement and measured stiffness on the IVD phantom.

II. 5 DOF MRE DRIVER POSITIONING ROBOT

A. Mechanical Design

The mechanical design of the MRE driver positioning system is based on a previously described 4-DOF robot [20]. The basic structure consists of a parallel plane mechanism for positioning co-linear ball joints. A fixed platform is made out of two parallel stages separated by rectangular pillars. In both the lower and

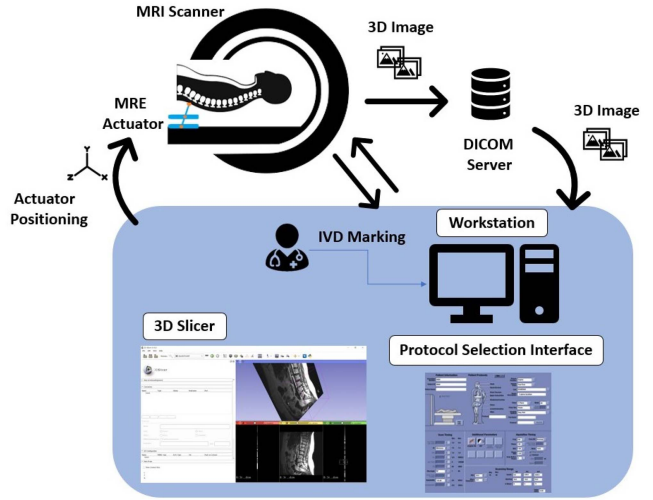


Fig. 1. Workflow of the proposed system. The position of the MRE driver is assessed and controlled by MRI feedback. 3D image volumes are constructed from the DICOM files obtained through T1-weighted scans. Based on the relative position of the MRE driver (piezo actuator) with respect to the imaging target (tissue mimicking phantom) the hydraulic actuators are driven to bring the MRE driver in contact with the imaging target. Then through MRE imaging, elastograms under various frequencies and harmonic loading orientations can be acquired.

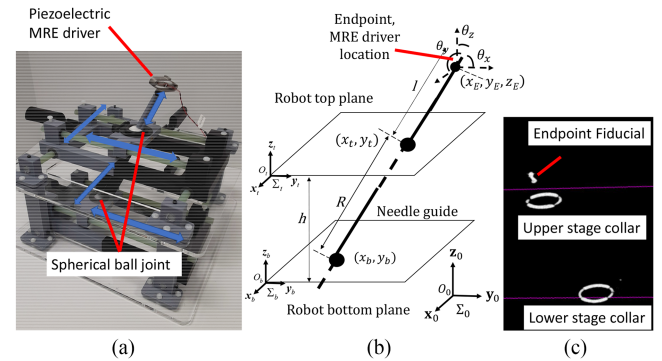


Fig. 2. 5 °-of-freedom MRE driver positioning unit (a) robot with actuators omitted for clarity. Motion directions depicted via blue arrows. (b) Kinematic diagram of the robot, the 6th DOF, rotation about the driver axis is not controlled. Σ_0 is the scanner/global coordinate frame, Σ_t and Σ_b are the top and bottom frames, misalignment between the 0 and t frames is described in Fig. 4, the top and bottom frames are assumed to only differ by a z direction translation of h . (c) Fiducial markers in processed morphological image, both endpoint and planar stage markers shown.

upper stages, identical carriers are used to provide motion along the y-axis. On top of the y-axis carriers, carriers providing motion along the x-axis are situated as shown in Fig. 2(a). Inside the x-axis carriers, a ring-shaped volume is left empty to create the fiducial marker. Furthermore, at the center of these x-axis carriers custom cut spherical ball joints are placed. The linear positioning of all the carriers is performed by hydraulic actuators (syringe-tube-syringe system). As the mechanical vibration source (MRE driver), a commercially available MR compatible piezo actuator (APA150M-NM, Cedrat Technologies) is used. This MRE driver is attached to the tip of the 5th axis which is passed through the upper spherical ball joint. The other end of the 5th axis is coupled with a syringe that serves as the 5th-DOF

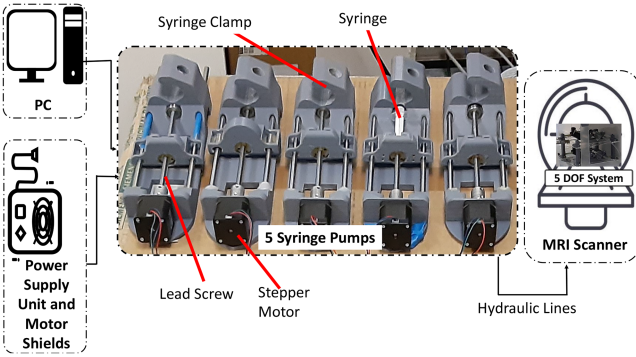


Fig. 3. Hydraulic actuator control system. The control system contains five syringe pumps, power supply unit which drives the NEMA 17 stepper motors, and a personal computer that runs the Arduino code to control the motion direction and step size of each stepper motor.

linear positioner. Within the aforementioned 5th axis, a fiducial marker is placed closer to its tip in which the piezo actuator is attached (see Fig. 2(c)). While the upper spherical ball joint serves as a guide for this 5th axis, the lower spherical ball joints holds the syringe tube casing which causes the 5th-DOF linear motion.

The robot is constructed almost entirely of polymer materials, with most parts 3D printed in PLA. Fasteners are nylon, and the hydraulic positioning actuators are made from plastic syringes. The only conductive materials placed in the scanner bore are the titanium shell of the APA piezoelectric actuator used as the MRE driver and its shielded wires.

B. Hydraulic Actuators

The positioning of the stage was accomplished by the use of open source linear hydraulic actuators [28]. The hydraulic actuator system consists of five syringes filled with hydraulic fluid, each attached to their own independent stepper motor that uses a lead screw to push or pull a block that compresses or extends the syringes as shown in Fig. 3. Four syringe pairs are allocated for motion control along the X and Y axes for the top and bottom plates, while the remaining syringe pair is used to push or pull the piezoelectric MRE driver towards/from the imaging target/tissue-mimicking phantom. Each syringe is connected by plastic tubing to an identical syringe that is fixed to the actuator frame.

In order to control the 5DOF MRE driver positioning unit, two 110V-to-12 V universal regulated switching power supply transformer are used. Nema 17 stepper motors ($1.8^\circ/\text{step}$) are connected to CNC shield expansion boards having stepper motor drivers with heat sinks as shown in Fig. 3. Then, through a custom written Arduino code, motion control of the stepper motors is performed via keyboard keys for clockwise and counter-clockwise rotation.

C. Kinematics and Fiducial Detection

The forward kinematics of the parallel stage platform is used for the mapping of the actuator positioning unit's configuration

to the MRE driver's position and orientation [20].

$$\begin{bmatrix} x_E \\ y_E \\ z_E \\ \theta_x \\ \theta_y \\ \theta_z \end{bmatrix} = \begin{bmatrix} -l(x_t - x_b)/R + x_b \\ -l(y_t - y_b)/R + y_b \\ -lh/R \\ \text{atan}2(y_t - y_b, h) \\ \text{atan}2(x_t - x_b, h) \\ \text{atan}2(y_t - y_b, x_t - x_b) \end{bmatrix}. \quad (1)$$

The hydraulic actuator positions connected to the top platform are described by x and y axis positions defined as x_t and y_t while for the hydraulic actuators connected to the bottom platform the x and y axis positions are described as x_b and y_b . The forward push distance of the MRE driver from the center of the upper ball joint is represented by l . The height between parallel stages/planes is h . The variables x , y , and z describe the position of the driver in the global fixed frame, while θ_x , θ_y , and θ_z describe the orientation of the driver in the global coordinate frame. All variables are shown in Fig. 2(b). From the definition of the rotations, it is clear that θ_x , θ_y , and θ_z are not independent. Once θ_x and θ_y are set by the positioning of x_t , y_t , x_b and y_b , θ_z is also defined and cannot be independently set. For this reason, only two angles are used to describe the robot configuration in the rest of this work, θ_x and θ_y .

The robot itself is not visible in MR images, and configuration must then be ascertained through the imaging of fiducial markers located on the collars and endpoint of the robot. The positions of the ring shaped collars inside the x-axis carriers and the fiducial markers at the tip of the connecting rod can be captured during the T1-weighted morphological scan after post-processing (Fig. 2(c)). Furthermore, within the field of view of this initial scan, the tissue mimicking phantom situated above the parallel stage mechanism can also be seen (see Fig. 2(a)). If the morphological scan data is pulled from the DICOM server to a local PC, this transferred image data, after thresholding, can be used to acquire the configuration of the robot given in (1)(see Fig. 2(c)). Finally, with the use of the aforementioned parameters one can calculate errors for each parameter listed as x_E , y_E , z_E , θ_x , θ_y .

III. IMAGE JACOBIAN BASED CONTROL IN MRI

A. Estimation of Image Jacobian Matrix

One practical method for controlling a system as depicted in the previous section in the absence of direct feedback for each hydraulic actuator is using an image Jacobian. An image Jacobian relates small displacements of a linear motor (in the current case the hydraulic actuator), to the motion of a fiducial within the field of view during image acquisition

$$\mathbf{J} = \frac{\partial \mathbf{C}}{\partial \mathbf{M}^T} \quad (2)$$

where \mathbf{C} is the configuration of the robot as measured by the detected fiducial locations, and \mathbf{M} is the actuator position, in steps. $\Delta\mathbf{C}$ and $\Delta\mathbf{M}$ are estimated by the change in pixels of the fiducial locations and the step commands sent to the motor.

The general case of convergence in image based Jacobian inverse control has been discussed at length, with singularity avoidance being the primary focus [29]. When a Jacobian matrix is estimated for a point in the workspace, and re-estimated when the actuator positioning unit's configuration changes, convergence is guaranteed for full rank Jacobians [29].

Jacobian based control through MRI faces challenges due to the feedback method. Image collection in typical RGB camera based control loops is near instantaneous, while in the MRI environment, a single image can take over 6 minutes to collect. The nature of the imaging system used here, the MRI scanner, disincentivizes re-estimation because of the significant time cost to do so. Because of this, the goal of this work is to select an image-guided control scheme that reduces the total scanner time, which may not have the fastest convergence in terms of position updates. This motivates the use of a Jacobian formulation that is applicable in the entire workspace, without re-estimation. Two forms of the Jacobian were explored for this robot, referred to below as the endpoint and planar Jacobians.

Observing that the image Jacobian entries corresponding to the 4 linear actuators do not change signs, a faster control methodology can be employed. The 4 DOF image jacobian can be estimated anywhere in the workspace, and used to control the ball joint locations, then the 5th DOF actuator can simply extend the MRE actuator to the target. While this work refers to the planar positioning method as a 4 DOF Jacobian, if the fiducials are mounted directly to each ball joint, the off diagonal sub-matrices of this matrix will be 0, leaving two independent matrices, one for each plane. This is because the motion of each ball joint is independent from the other. This method allows the Jacobian to only be estimated once, a significant saving of scanner time. The control methods evaluated above both achieved satisfactory positioning and orientation accuracy, but the two phase approach does not have the stability drawbacks of the endpoint based method.

B. Feasibility of Endpoint Jacobian Based Control

The convergence of the Jacobian based control method is restricted by the choice of C . Particularly around the configurations most likely to be chosen, namely those in which the MRE actuator is nearly vertical in this particular application. When the Jacobian matrix is chosen to map actuation to MRE driver motion, the Jacobian matrix is determined by $C = [x_E \ y_E \ z_E \ \theta_x \ \theta_y]^T$, the 5 DOF configuration of a fiducial marker in the image space, and $M = [M_{xt} \ M_{yt} \ M_{xb} \ M_{yb} \ M_l]^T$, the five hydraulic actuator positions in the 5-DOF MRE actuator positioning unit space. Since the fiducials are encapsulated at the tip of the extension rod (i.e., fixed in position within the component), this Jacobian matrix also relates the driver position to the positioning unit's orientation. The full 5×5 Jacobian matrix is shown in A1. Note that while all six variables defined for the driver options and orientations are measurable, as (1) shows, the six output variables are only functions of five motor positions, with the z axis rotation fully defined by θ_x and θ_y , as described in II-C.

From the terms that map to endpoint Z motion, it is clear that this Jacobian will only work under specific conditions. Particularly, when the posture is vertical, (i.e $x_b = x_t$ or $y_b = y_t$) the signs of many of the entries flip. This creates 4 quadrants in the workspace, defined by the possible combinations of $sgn(x_b - x_t)$ and $sgn(y_b - y_t)$. For instance, the sign of the top right element, $\frac{x_b - x_t}{R}$, follows with $sgn(x_b - x_t)$ this results in incorrectly computed updates if the Jacobian is not re-estimated often enough to capture the changes in quadrant. While this re-estimation is feasible in camera based control methods, in the MRI, frequent re-estimation is not possible because of the time cost incurred.

In the case of MRE orientation, it is desirable to locate the actuator perpendicular to the target, which will likely mean configurations that are near the problem configurations. For that reason, the use of the end-point Jacobian for position control in MRI is not suitable. As an alternative, the following planar method is proposed.

IV. STABILITY OF IMAGE GUIDED CONTROL USING PLANAR JACOBIAN

A. Planar Jacobian

As shown in the preceding section, the endpoint based Jacobian suffers from a singularity in the center of the most likely desirable configuration. Because the actuators operate independently, it is possible to define a Jacobian matrix where this is avoided. The parallel plane structure of the robot lends itself well to the use of a Jacobian in which the first 4 entries represent the x and y positions of each of the collars without causing a singularity problem within its workspace. The fifth entry can be defined by the distance between the top collar and the MRE driver fiducial, but is left out of the following analysis for simplicity, as it does not impact the other 4.

The ideal planar Jacobian \tilde{J}_p representing the MRE driver's location and fiducial markers co-located with the upper and lower ball joints, $C = [x_t \ y_t \ x_b \ y_b]^T$, is defined by the motion of each hydraulic actuator:

$$\Delta C = \tilde{J}_p \Delta M \quad (3)$$

$$\tilde{J}_p = \begin{pmatrix} s_{xt}(x_t, y_t) & 0 & 0 & 0 \\ 0 & s_{yt}(x_t, y_t) & 0 & 0 \\ 0 & 0 & s_{xb}(x_b, y_b) & 0 \\ 0 & 0 & 0 & s_{yb}(x_b, y_b) \end{pmatrix} \quad (4)$$

where s represents distance per step in units of pixels/step with a subscript for each of the 4 axes of two parallel stages. Friction is the primary driver of variability in s , and as stage location is dictated by the position of each axis on a guide rod, s varies with the robot configuration, as described in Assumption 1. For example, the top plane position increments are given in a decoupled form: $\Delta x_t = s_{xt} \Delta M_{xt}$, $\Delta y_t = s_{yt} \Delta M_{yt}$, where ΔM_{xt} and ΔM_{yt} are increments for hydraulic actuator positions.

The structure of \tilde{J}_p has two major differences from that of J_E . Firstly, alignment of the actuator positioning unit and the scanner frames is assumed. Secondly, the coefficients are

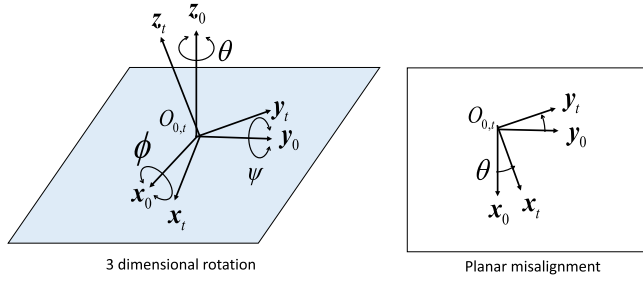


Fig. 4. Small rotation about 3 axes between coordinate frames. The right side shows the projection of the new rotated axes into the scanner image plane, a rotation captured by only θ , the rotation about the Z axis.

treated as constants, but in reality may vary significantly in magnitude through the workspace as hydraulic actuator step sizes are friction dependent. The following assumptions are made about the system.

Assumption 1: The actuators vary in step size with friction as s is a function of position (i.e., $s_{xt} = s_{xt}(x_t, y_t)$, $s_{yt} = s_{yt}(x_t, y_t)$). Calibration before use provides the user with their distributions.

Assumption 2: The actuator step direction does not change, (e.g., a given command will produce motion in the same direction throughout the workspace).

Assumption 3: The robot's frame is rigid, with a small, fixed angle rotation from the scanner coordinates as misalignment, as shown in Fig. 4.

Assumption 1 requires the user to use their nominal values (typically, constants) in practice. Assumption 2 guarantees that the ratio $\frac{s}{\dot{s}}$ is always positive. Assumption 3 enables the use of a single angular rotation to describe the transformation between the robot and MRI frames.

This is demonstrated for one of the 2-DOF stages, as follows. For example, using the z-y-x Euler angle convention, with respective rotations of θ , ψ , and ϕ , the rotation matrix between robot and MRI frames, R_{zyx} , becomes

$$\mathbf{R}_{zyx} = \begin{bmatrix} c_\theta c_\psi & c_\theta s_\psi s_\phi - s_\theta c_\phi & c_\theta s_\psi s_\phi + s_\theta c_\phi \\ s_\theta c_\psi & s_\theta s_\psi s_\phi + c_\theta c_\psi & s_\theta s_\psi s_\phi - c_\theta c_\psi \\ -s_\psi & c_\psi s_\phi & c_\psi c_\phi \end{bmatrix} \quad (5)$$

where s and c represent sin and cos respectively. Only the left 2 rows and columns are salient, as the 2 DOF planar measurements do not capture motion in the z (vertical) axis. For small angles, and planar projections, (5) can then be approximated by the 2 DOF planar rotation matrix R_{p2} :

$$\begin{bmatrix} x_t \\ y_t \end{bmatrix} = R_{p2} \begin{bmatrix} x_0 \\ y_0 \end{bmatrix} \approx \begin{bmatrix} 1 & -\theta \\ \theta & 1 \end{bmatrix} \begin{bmatrix} x_0 \\ y_0 \end{bmatrix} \quad (6)$$

which follows the form of a single, z axis rotation, of Σ_t with respect to Σ_0 . This rotation matrix also applies to the lower plane coordinate frame Σ_b . From (4), the true planar Jacobian matrix with a small angle rotation R_{p2} is represented

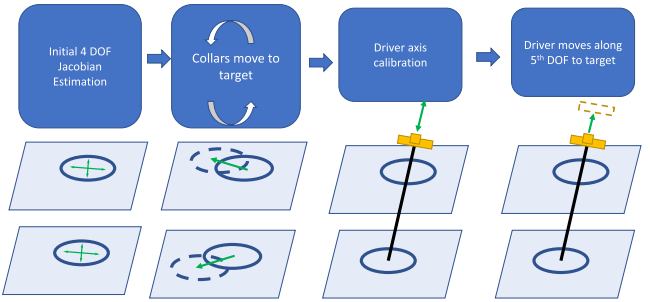


Fig. 5. Two stage driver positioning process. The initial estimation and positioning takes place in the 2 planes, with the 5th DOF extension occurring afterwards.

as $\text{diag}[R_{p2}, R_{p2}] \tilde{\mathbf{J}}_p$, or:

$$\mathbf{J}_p = \begin{pmatrix} s_{xt} & -s_{xt}\theta & 0 & 0 \\ s_{yt}\theta & s_{yt} & 0 & 0 \\ 0 & 0 & s_{xb} & -s_{xb}\theta \\ 0 & 0 & s_{yb}\theta & s_{yb} \end{pmatrix} \quad (7)$$

A general image Jacobian estimation method will provide an estimate of (7):

$$\begin{aligned} \hat{\mathbf{J}}_p &= \text{diag}[R_{p2}, R_{p2}] \text{diag}[\hat{s}_{xt}, \hat{s}_{yt}, \hat{s}_{xb}, \hat{s}_{yb}] \\ &= \begin{pmatrix} \hat{s}_{xt} & -\hat{s}_{xt}\theta & 0 & 0 \\ \hat{s}_{yt}\theta & \hat{s}_{yt} & 0 & 0 \\ 0 & 0 & \hat{s}_{xb} & -\hat{s}_{xb}\theta \\ 0 & 0 & \hat{s}_{yb}\theta & \hat{s}_{yb} \end{pmatrix} \end{aligned} \quad (8)$$

where \hat{s}_* is an estimation of each s_* at the Jacobian estimation point. Note that each of non-zero elements is only numerically estimated without separating θ and step distance values. As discussed in III, $\hat{\mathbf{J}}_p$ cannot be frequently updated in MRI. It is desired that $\hat{\mathbf{J}}_p$ is estimated only once at a certain point in the workspace, and is used throughout the visual navigation as a constant.

B. Control Method

Fig. 5 shows the planned control method to produce 5 DOF positioning of the MRE driver in a 2 stage process. First, the two parallel plane actuators are controlled with a 4 DOF Jacobian to move the ball joint collars to a target position. Second, the driver axis actuator is advanced to move the driver into contact with the skin and complete the positioning. This process can be used to effectively position the driver very close to the final target position.

This scheme leverages the easily guaranteeable convergence of the planar Jacobian method above. Benchtop experiments were carried out to confirm the functionality of this approach. Performance was also compared to the endpoint based method.

C. Convergence Analysis

This section will verify the stability and robustness of the planar Jacobian based approach. See Appendix A for 1 DOF stability analysis that will be extended to the planer case.

For a given image Jacobian matrix estimate, $\hat{\mathbf{J}}_p$, the hydraulic actuator commands, $\Delta \mathbf{M}_k$ at the k -th iteration can be found by the error, $\mathbf{e}_k = \mathbf{C}_d - \mathbf{C}_k$,

$$\Delta \mathbf{M}_k = \alpha \hat{\mathbf{J}}_p^{-1} \mathbf{e}_k. \quad (9)$$

where $\mathbf{C}_d^{4 \times 1}$ is a vector with the desired x-y stage positions. Without the loss of generality, $\mathbf{C}_d = [0, 0, 0, 0]^T$ can be used for stability analysis.

Theorem 1: A choice of the feedback gain α within the range of $0 < \alpha < \min\left\{\frac{2\hat{s}_{xt}}{\max s_{xt}(x_t, y_t)}, \frac{2\hat{s}_{yt}}{\max s_{yt}(x_t, y_t)}, \frac{2\hat{s}_{xb}}{\max s_{xb}(x_b, y_b)}, \frac{2\hat{s}_{yb}}{\max s_{yb}(x_b, y_b)}\right\}$ guarantees asymptotic convergence of the error in position for the control law (9), $\mathbf{e}_k \rightarrow 0, k \rightarrow \infty$.

The error dynamics is given as

$$\begin{aligned} \Delta \mathbf{M}_k &= -\mathbf{J}_p \alpha \hat{\mathbf{J}}_p^{-1} \mathbf{M}_k = -\begin{bmatrix} \mathbf{R}_{p2} & O \\ O & \mathbf{R}_{p2} \end{bmatrix} \tilde{\mathbf{J}}_p \alpha \\ &\times \left\{ \begin{bmatrix} \mathbf{R}_{p2} & O \\ O & \mathbf{R}_{p2} \end{bmatrix} \text{diag}[\hat{s}_{xt}, \hat{s}_{yt}, \hat{s}_{xb}, \hat{s}_{yb}] \right\}^{-1} \mathbf{e}_k \\ &= -\alpha \begin{bmatrix} \frac{\hat{s}_{xt}}{\hat{s}_{xt}} x_{tk} \\ \frac{\hat{s}_{xt}}{\hat{s}_{yt}} y_{tk} \\ \frac{\hat{s}_{yt}}{\hat{s}_{yt}} x_{bk} \\ \frac{\hat{s}_{yt}}{\hat{s}_{yb}} y_{bk} \end{bmatrix}. \end{aligned} \quad (10)$$

The proof of stability in Appendix A applies to each of the positions, resulting in the stability of the 4 DOF planar case, $x_{tk} \rightarrow 0, y_{tk} \rightarrow 0, x_{bk} \rightarrow 0, y_{bk} \rightarrow 0, k \rightarrow \infty$. Since a scalar gain $\alpha > 0$ is used in the control law, its upper bound is the lowest among $\frac{2\hat{s}_{xt}}{\max s_{xt}(x_t, y_t)}, \frac{2\hat{s}_{yt}}{\max s_{yt}(x_t, y_t)}, \frac{2\hat{s}_{xb}}{\max s_{xb}(x_b, y_b)}, \frac{2\hat{s}_{yb}}{\max s_{yb}(x_b, y_b)}$, to be sufficiently conservative.

D. Benchtop Position Control Experiments

The control configuration of a 4 DOF planar positioning step, with advancement of the 5th DOF actuator as the final step was evaluated, as described in Section IV-B. Planar positions were measured via an RGB-D camera (Intel Realsense). In this case, a 4 DOF image jacobian relating the planar position of each ball joint to the motion of the linear piezo actuators was used. After each ball joint reached the desired location, the 5th DOF DC linear actuator was extended to place the endpoint at the target location. Location and orientation accuracy were measured via the visual fiducial shown in Fig. 6. In the benchtop experiments reported, target locations and endpoint locations were experimentally determined prior to beginning the experiments, because of visual occlusion caused by multiple components of the robot. In the MRI scanner, only the fiducials are visible, so target locations for the ball joints can be computed from a desired endpoint location and orientation.

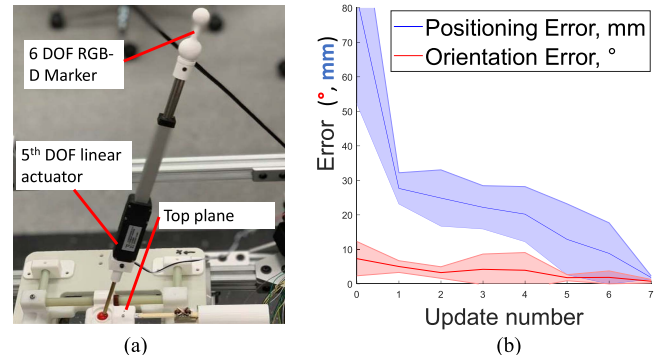


Fig. 6. Benchtop positioning experimental setup (a) and results (b). The 5th DOF DC linear actuator was extended to place the endpoint at the target which helps to measure the accuracy of the location and orientation. Endpoint position and orientation were found via the center positions of the two spheres. In B, both position and orientation error are shown to be satisfactory after 7 iterations of the control law. The 4DOF positioning phase was completed first, with the 5th DOF extension to the target occurring after the upper and lower positions were reached.

Positioning results for the benchtop experiments are shown in Fig. 6(b). For the 4 + 1 control method, final mean error was 1.8 mm and 0.78 degrees.

V. MRI EXPERIMENTS

A. Phantom Preparation

A tissue mimicking gelatin phantom was prepared to evaluate the positioning mechanism. Three disc shaped phantoms made out of a 20:100 gelatin-to-water mixture were placed inside of a 7:100 gelatin-to-water mixture. A 2 mm plastic rod is passed through the disc shaped phantoms to hold them in place as shown in Fig. 7(b). During the preparation of both mixtures, gelatin dissolved in water is heated for 80 seconds and then placed in a vacuum chamber for 30 seconds before being poured into molds. A rectangular phantom was used in this work, as the primary aim of the work was the demonstration of the positioning system, rather than investigation of the IVD itself.

B. MR Imaging

As described in Section IV, the desired positions of the robot are difficult to reach with a traditional endpoint based visual servoing method, but can be readily achieved using the 4+1 method described in IV-B. Experimental evaluation in the MRI took place at the three configurations shown in Fig. 7(c) that were reached through manually determined jogging of the hydraulic actuators, but that are achievable via the 4 + 1 visual servoing method.

Experimental testing and evaluation of the prototype system was performed in a 3-tesla MRI (Siemens Trio), as shown in Fig. 7. The 5 DOF MRE actuator positioning unit was positioned beneath a phantom holder (see Fig. 7(b)), which contains the tissue mimicking gelatin, with a spine RF coil placed above it. T1-weighted morphological and MR Elastography scans were utilized, with the morphological scans providing the 5DOF

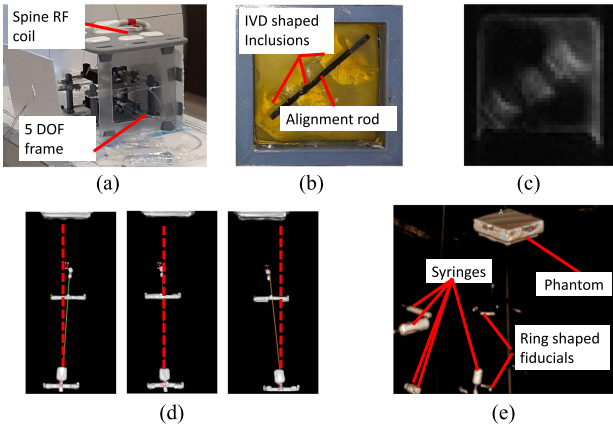


Fig. 7. Experimental setup and images. (a) This setup is evaluated within a 3-tesla MRI Scanner (Siemens Trio). The phantom is placed above the 5 DOF frame and the coil is placed on top of the phantom structure. (b) Gel Phantom(bottom view, mirrored for clarity),Three disc inclusions, stiffer than the surrounding gel, are placed along the diagonal. A thin plastic rod passes through each disc to maintain alignment. (c) Magnitude image of the phantom. (d) Sagittal view of 3 different robot configurations. Within the field of view end point fiducials, ring shaped collars, and the tissue mimicking phantom are visible. The robot orientation for the left, middle and right figure is -5° , 0° , and 6° respectively. (e) Representative morphological image.

unit's configuration confirmation. A representative morphological scan is shown in Fig. 7(d). MRE scans were performed for 3 different actuator positioning unit configurations. For all configurations, the MRE data was acquired for 19 slices with 3D motion encoding gradients using echo planar spin echo 2D pulse sequence in axial planes with the following imaging parameters: acquisition matrix = 96×48 , flip angle = 90, FOV = 96×192 mm, 8 phase offsets, slice thickness = 2 mm, gradient amplitude = 40 mT/m, mechanical vibration frequencies of 30 Hz (TE = 100 ms, TR = 3803 ms), 60 Hz (TE = 59 ms, TR = 2541.4 ms), and 90 Hz (TE = 45 ms, TR = 1901.5 ms).

C. Image Quality

Because of the addition of the small titanium MRE driver shell, and associated driving wires, the signal to noise ratio in a magnitude image of the phantom with the robot was checked. The SNR was measured as the mean intensity in the phantom divided by the standard deviation in air, this was 1222, indicating that the images are of sufficient quality with the robot in place below the phantom. No distortion or other visual effects were observed due to the robot, likely due to the primarily polymer construction.

D. MRE Results

Locations of the fiducials, ring shaped collars, and the tissue mimicking phantom are captured through the T1-weighted morphological scan. In 3D Slicer, after volume rendering and thresholding, centers of the end fiducial and the lower collar are marked. A line is drawn through these markers to show the orientation differences among the three different configurations (see Fig. 7(c)). For these 3 different configurations, wave field data for

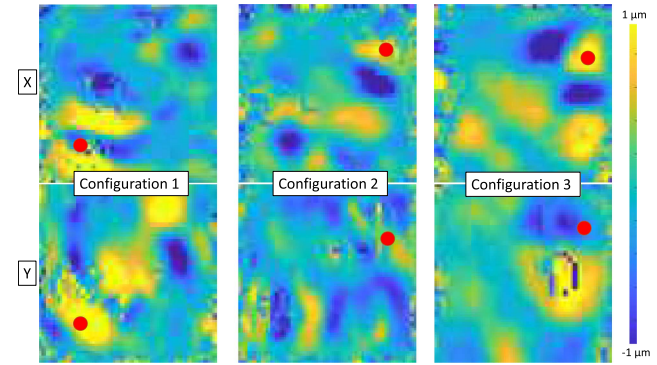


Fig. 8. Displacement fields for 3 different robot configurations under 90 Hz vibration, 5th slice. Top row shows the displacement fields in units of micrometer for motion encoding along X axis while bottom row shows for the motion encoding along Y axis. Within each figure, the MRE driver contact point is shown by the red dots.

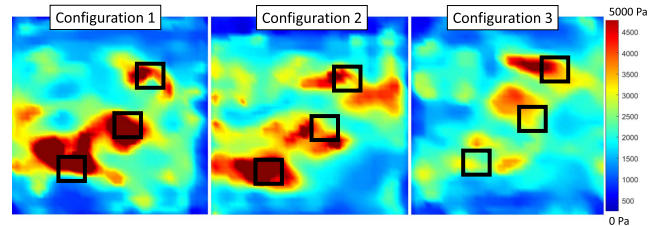


Fig. 9. Elastograms for the 3 different robot configurations with 90 Hz vibration. Within each elastogram, 3 different 9-by-9 pixel ROIs are selected along the diagonal at the location of each phantom disc in the 5th image plane.

the X and Y motion encoding directions at 90 Hz of vibration are depicted in Fig. 8. The displacement data shown in Fig. 8 is for slice 5. Octahedral shear stress signal to noise ratio (OSS-SNR) for the same slice is shown in Fig. 10(a). From these wave field data, elastograms are acquired as shown in Fig. 9. The inversion was performed using the algebraic inversion method described by Oliphant *et al.* [30]. Finally, within each elastogram, mean stiffness for three different 3-by-3 pixel ROIs is calculated and plotted in Fig. 10(b). Paired t tests were used to compare the mean OSS-SNR and estimated stiffness across configurations for each region, with significant differences found for at least one configuration pair for each location, after a Bonferroni correction ($\alpha = \frac{\alpha}{9}$). All 18 p values are listed in Tables I and II.

VI. DISCUSSION

A. Image Jacobian Control

As shown in Fig. 6(b), the use of a single estimated Jacobian along with the planar positioning method enabled 5 DOF control of the robot, with satisfactory final errors in both position and orientation. Differences between the estimated and actual Jacobian are acceptable, as the form chosen produces a stable controller if angular misalignment is small and gains are chosen correctly. The planar image Jacobian method is effective for small rotational misalignment about the x and y axes, which is easy to ensure with manual placement of the robot

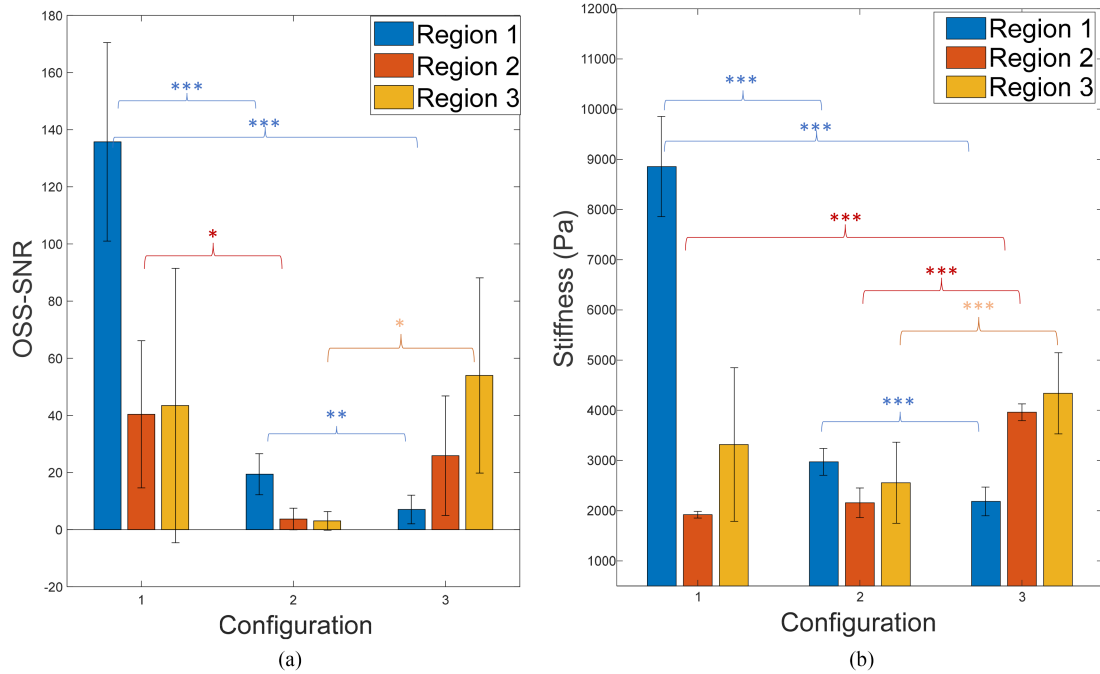


Fig. 10. Mean MRI results, Octahedral Shear Strain (OSS) SNR and shear stiffness. **(a)** Shows OSS-SNR across the 3 configurations and regions of interest, **(b)** gives the computed mean shear stiffness of the same regions, stars represent mean difference significance levels corrected for 9 tests.

within the scanner bore. Although the final accuracy is limited by factors between the endpoint and drive (such as bending of the driver axis rod), accuracy was certainly sufficient for MRE.

As described above, MRE of the IVD necessitates configurations that are vertical, or near vertical, challenging the use of an endpoint based servoing method. However, other tissues or patient configurations, particularly those in which the quadrant of the target configuration is known ahead of time, could use the endpoint Jacobian and positioning method. If $\text{sgn}(x_b - x_t)$ and $\text{sgn}(y_b - y_t)$ are known prior to beginning the scan, sign errors in the estimated Jacobian can be avoided altogether.

B. MRE Results

While previous work has primarily focused on liver or breast, the IVD is one of the critical targets for MRE interrogation. Degeneration of the IVD is often accompanied by structural changes, especially in the nucleus pulposus [31]. This has made the IVD and nucleus pulposus a target for MRE study. Previous research demonstrated the ability of MRE to distinguish between normal, mild, and severe degeneration of IVD [25]. Measurement of displacements transferred to spine under different preloading conditions will enable early diagnosis of potential degenerative disc disease, which is the primary cause of chronic back pain or low back pain. The small size of the IVD, along with the relatively high stiffness and shallow depth indicate that higher frequency excitation will result in improved elasticity measurements. Ex vivo MRE done on baboon spine

at 1–1.5 kHz showed promising results, but actuation developments are needed to obtain high-frequency results in vivo [26]. Walter *et al.* benefited from MRE acquired shear stiffness as a biomarker to provide the state of disc degeneration [9]. In the study conducted by Beauchemin *et al.*, bovine IVD showed an increasing trend in stiffness as the actuation frequency was increased from 1000 to 1800 Hz [27]. This frequency dependence of an intrinsic mechanical property is an artefact of the actuation methodology, and must be solved to produce reliable measurements of IVD stiffness.

As can be seen from Fig. 9, the positioning and orientation of the MRE driver causes significant differences in the acquired elastograms. The mean octahedral shear strain (OSS) SNR results shown in Fig. 10(a), also reflect the effect of configuration on MRE confidence. This is particularly important due to the large degree of attenuation at high frequencies in human tissue [32].

It should be noted that this work did not seek to evaluate the absolute accuracy of the IVD property estimation. Rather, statistically significant differences in estimated modulus across robot configurations were the main points of interest. If the estimated stiffness varies for each of the configurations, it follows that configuration impacts stiffness accuracy.

If a fixed actuator configuration were to be used with this phantom, at least one of the 3 discs would be measured at a relatively lower OSS-SNR, and consequently an incorrect stiffness would be estimated. Taking configuration 3 as an example, the SNR decreases from 54 to only 7 as the ROI moves away from the contact point. This impacts the estimated stiffness as

TABLE I

STATISTICAL SIGNIFICANCE OF MEAN DIFFERENCES IN OSS-SNR, ACROSS CONFIGURATION BOLD ENTRIES ARE STATISTICALLY SIGNIFICANT WITH THE CORRECTED ALPHA VALUE OF .0056

	Configurations		
	1 and 2	1 and 3	2 and 3
Location 1	p = .000020	p = .0000064	p = .00046
Location 2	p = .0018	p = .13	p = .013
Location 3	p = .034	p = .56	p = .0015

TABLE II

STATISTICAL SIGNIFICANCE OF MEAN DIFFERENCES IN SHEAR STIFFNESS, ACROSS CONFIGURATION, BOLD ENTRIES ARE STATISTICALLY SIGNIFICANT WITH THE CORRECTED ALPHA VALUE OF .0056

	Configurations		
	1 and 2	1 and 3	2 and 3
Location 1	p = .00000039	p = .00000013	p = .000000016
Location 2	p = .056	p = .000000015	p = .00000079
Location 3	p = .024	p = .017	p = .0000096

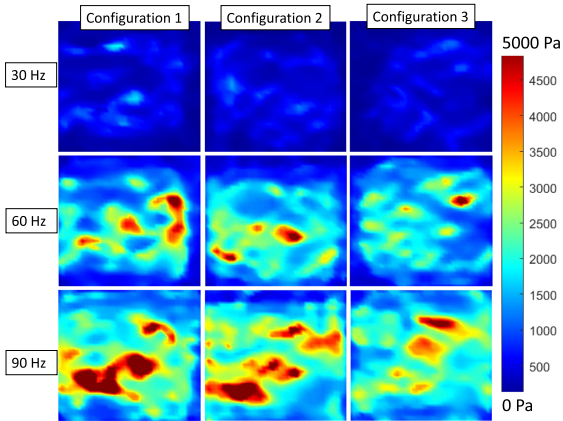


Fig. 11. Elastograms for the 3 different configurations. Driver actuation frequencies of 30, 60, and 90 Hz, results shown in the 5th imaging plane.

well, with ROI 1 recording an estimate of 2.1 kPa, less than 25% of the value in the highest OSS-SNR configuration (8.8 kPa in configuration 1). It is then important to consider configuration of the MRE driver, even in situations where the OSS-SNR appears to be suitably large.

In the case of performing MRE throughout the whole lumbar section of a patient for the detection of disc degeneration, proper alignment of the driver becomes more important. Because shear wave attenuation caused by improper positioning of the driver with respect to the targeted intervertebral disc will provide misleading shear stiffness information. Furthermore, soft tissues show viscoelastic behavior, and multi-frequency characterization via MRE is a must. For instance, disc inclusions cannot be distinguished at 30 Hz and 60 Hz elastograms as clearly as in the case of 90 Hz elastograms (see Fig. 11, in the appendix). In addition to multi-frequency characterization, multi-directional MRE is required too for proper characterization of the mechanical properties of a soft tissue/tissue-mimicking phantom.

In Fig. 10, it is shown that for the same ROI, the acquired mean stiffness value can triple as in the case of configuration 1. Moreover, for proper control of the driver's position accurate visualization of the end fiducials and the ring shape collars is required. The current setup tested experienced leakage from the 3D printed components. To avoid this, instead of using a fluid type contrast agent a more durable material such as silicon can be chosen. For patient comfort, instead of piezo actuator, a pressure wave driven soft cushion unit can be preferred. Performing MRE for the whole lumbar region can be accomplished without any interference from the MRI technician thanks to visual servoing.

Fig. 9 and 10 show the clear differences in both image quality and measured stiffness in specific ROIs achieved by varying the contact location and angle of the MRE driver. This result has not previously been demonstrated in MRE, and the applications are numerous. In particular the ability to control OSS-SNR by varying the actuator configuration will enable more accurate interrogation of smaller ROIs. Modulation of the wave field will also enable realization of other advanced MRE techniques to investigate smaller and stiffer tissues located in regions of the body beyond the reach of traditional driver technologies.

C. Future Work

Although this work focused on the use of this positioning system to configure a piezoelectric MRE driver, the application of the positioning system is not exclusive to any actuator type. The small size of the piezoelectric actuators make them good candidates for use with the robot, and standard pneumatic cushion type actuators may be too large. However, some novel rotary actuators [33], would also be potential candidate drivers for this type of positioning system.

D. Limitations

This work was limited to the investigation of Jacobian structure on control method selection and the MRE imaging of a gelatin phantom. Future work should provide closed-loop positioning and imaging performance baselines, as well as the use of this positioning method on human subjects.

VII. CONCLUSION

This work developed, tested, and evaluated a new actuator positioning system for MR Elastography imaging. It becomes apparent that multi-directional multi-frequency MRE will provide a more reliable shear stiffness information for the mechanical characterization of soft tissues. This initial prototype paves the way for the development of a semi-automatic system to be used during the identification of the level of disc degeneration in patients having low back pain. Hopefully, in addition to Pfirrmann scoring, elastograms of IVDs will be used for identifying the level of disc degeneration in clinical practice.

$$\mathbf{J}_E = \begin{pmatrix} \frac{l(x_b-x_t)^2}{R^3} - \frac{l}{R} & \frac{l}{R} - \frac{l(x_b-x_t)^2}{R^3} + 1 & \frac{l(y_b-y_t)(x_b-x_t)}{R^3} & -\frac{l(y_b-y_t)(x_b-x_t)}{R^3} & \frac{x_b-x_t}{R} \\ \frac{l(x_b-x_t)(y_b-y_t)}{R^3} & -\frac{l(x_b-x_t)(y_b-y_t)}{R^3} & \frac{l(y_b-y_t)^2}{R^3} & -\frac{l}{R} \frac{l}{R} - \frac{l(y_b-y_t)^2}{R^3} + 1 & \frac{y_b-y_t}{R} \\ -\frac{hl(x_b-x_t)}{R^3} & \frac{hl(x_b-x_t)}{R^3} & -\frac{hl(y_b-y_t)}{R^3} & \frac{hl(y_b-y_t)}{R^3} & -\frac{h}{R} \\ 0 & 0 & \frac{h}{(y_b-y_t)^2+h^2} & -\frac{h}{(y_b-y_t)^2+h^2} & 0 \\ \frac{h}{(x_b-x_t)^2+h^2} & -\frac{h}{(x_b-x_t)^2+h^2} & 0 & 0 & 0 \end{pmatrix} \quad (11)$$

APPENDIX

A. End-Point Jacobian Matrix

The full end-point Jacobian matrix, \mathbf{J}_E is shown in (11) at the top of this page.

B. Stability of Iterative 1 DOF Position Control With a Conservative Fixed Gain

The stability of a single axis discrete-time position control is assessed here, and extended to multiple-axis visual servoing control in IV. Consider a control law in which updates in the k -th iteration for the x axis position are computed by

$$u_k = \alpha \frac{e_k}{\hat{s}} \quad (12)$$

where u_k is the motor step command, $\alpha > 0$ is a feedback gain, and $e_k = x_d - x_k$ is the error in position. $\hat{s} > 0$ is the nominal step distance of the actuator within the range of motion chosen as a constant. Without the loss of generality, the desired position can be given as $x_d = 0$. The control law then becomes $u_k = \alpha x_k / \hat{s}$. The actual motion of the robot, $x_{k+1} = x_k + \Delta x_k$, will be generated by the true step distance $s(x_k)$, instead of estimated \hat{s} ,

$$\Delta x_k = s(x_k) u_k = -\alpha \frac{s(x_k)}{\hat{s}}, \quad (13)$$

where the true step distance $s(x_k)$ may vary due to friction that is usually position dependent.

Theorem 2: A choice of the feedback gain within the range of $0 < \alpha < \frac{2\hat{s}}{\max s(x_k)}$ guarantees asymptotic convergence of the error in position, $e_k \rightarrow 0, k \rightarrow \infty$.

Proof: Consider a Lyapunov function candidate, and its difference,

$$L_k = e_k^2 = x_k^2 > 0 \quad (14)$$

$$\Delta L = L_{k+1} - L_k = x_{k+1}^2 - x_k^2. \quad (15)$$

Substituting the expression for x_{k+1} yields

$$\Delta L = \left\{ \left(1 - \frac{\alpha s(x_k)}{\hat{s}} \right)^2 - 1 \right\} x_k^2, \quad (16)$$

resulting in the condition that ΔL is negative definite if,

$$\left| 1 - \frac{\alpha s(x_k)}{\hat{s}} \right| < 1 \quad (17)$$

or equivalently $0 < \alpha < \frac{2\hat{s}}{s(x_k)}$ for all possible $s(x_k)$ within the range of motion. Thus, stability of a single axis with a nominal step distance can be guaranteed if $\max s(x_k)$ is known, and α is chosen conservatively. Friction in the axis itself if the primary cause of the variability in s , and as such, this ratio can be obtained experimentally, as was done in prior work [20]. Because uncertainty in s stems from frictional forces, the known fixed-free step size serves as an upper bound on s , and frictional reductions can be estimated or experimentally determined.

C. Full MRE Results

The results of all 9 MRE images are shown in Fig. 11. With the best definition of the IVD shaped phantom inclusions shown in the 90 Hz images, and clear configuration dependence. Results from a paired t-test across different configurations are shown in Tables I and II.

ACKNOWLEDGMENT

The authors would like to thank Kamil Banibaker and Dewey Chu for their support during the experiments.

REFERENCES

- [1] Y. S. Choi, "Pathophysiology of degenerative disc disease," *Asian Spine J.*, vol. 3, no. 1, pp. 39–44, 2009.
- [2] N. A. Farshad-Amacker *et al.*, "MR imaging of degenerative disc disease," *Eur. J. Radiol.*, vol. 84, no. 9, pp. 1768–1776, 2015.
- [3] N. A. Farshad-Amacker *et al.*, "The intervertebral disc, the endplates and the vertebral bone marrow as a unit in the process of degeneration," *Eur. Radiol.*, vol. 27, no. 6, pp. 2507–2520, 2017.
- [4] C. Paul *et al.*, "Quantitative MRI in early intervertebral disc degeneration: T1rho correlates better than T2 and ADC with biomechanics, histology and matrix content," *PLoS One*, vol. 13, no. 1, 2018, Art. no. e0191442.
- [5] J. Y. Hon *et al.*, "In vivo quantification of lumbar disc degeneration: Assessment of ADC value using a degenerative scoring system based on pfirrmann framework," *Eur. Spine J.*, vol. 24, no. 11, pp. 2442–2448, 2015.
- [6] J. P. Jarman *et al.*, "Intervertebral disc height loss demonstrates the threshold of major pathological changes during degeneration," *Eur. Spine J.*, vol. 24, no. 9, pp. 1944–1950, 2015.
- [7] R. Muthupillai *et al.*, "Magnetic resonance imaging of transverse acoustic strain waves," *Magn. Reson. Med.*, vol. 36, no. 2, pp. 266–274, 1996.
- [8] K. J. Streitberger *et al.*, "In vivo multifrequency magnetic resonance elastography of the human intervertebral disk," *Magn. Reson. Med.*, vol. 74, no. 5, pp. 1380–1387, 2015.
- [9] B. A. Walter *et al.*, "MR elastography-derived stiffness: A biomarker for intervertebral disc degeneration," *Radiology*, vol. 285, no. 1, pp. 167–175, 2017.
- [10] Y. Zheng *et al.*, "Magnetic resonance elastography with twin drivers for high homogeneity and sensitivity," in *Proc. Int. Conf. IEEE Eng. Med. Biol. Soc.*, 2006, pp. 1916–1919.

- [11] Y. Zheng *et al.*, "Magnetic resonance elastography with twin pneumatic drivers for wave compensation," in *Proc. 29th Annu. Int. Conf. IEEE Eng. Med. Biol. Soc.*, 2007, pp. 2611–2613.
- [12] Y. K. Mariappan *et al.*, "Magnetic resonance elastography with a phased-array acoustic driver system," *Magn. Reson. Med.: An Official J. Int. Soc. Magn. Reson. Med.*, vol. 61, no. 3, pp. 678–685, 2009.
- [13] W. Neumann *et al.*, "Coupled actuators with a mechanically synchronized phase during mr elastography: A phantom feasibility study," *Concepts Magn. Reson. Part B: Magn. Reson. Eng.*, vol. 48, no. 4, 2018, Art. no. e21403.
- [14] A. T. Anderson *et al.*, "Observation of direction-dependent mechanical properties in the human brain with multi-excitation mr elastography," *J. Mech. Behav. Biomed. Mater.*, vol. 59, pp. 538–546, 2016.
- [15] C. Stüer *et al.*, "Robotic technology in spine surgery: Current applications and future developments," in *Intraoperative Imaging*. Berlin, Germany: Springer, 2011, pp. 241–245.
- [16] F. Roser *et al.*, "Spinal robotics: Current applications and future perspectives," *Neurosurgery*, vol. 72, no. suppl_1, pp. A 12–A18, 2013.
- [17] A. Bertelsen *et al.*, "A review of surgical robots for spinal interventions," *Int. J. Med. Robot. Comput. Assist. Surg.*, vol. 9, no. 4, pp. 407–422, 2013.
- [18] S. C. Overley *et al.*, "Navigation and robotics in spinal surgery: Where are we now?," *Neurosurgery*, vol. 80, no. 3S, pp. S86–S99, 2017.
- [19] J. Huang *et al.*, "Spine surgical robotics: Review of the current application and disadvantages for future perspectives," *J. Robotic Surg.*, vol. 14, no. 1, pp. 11–16, 2020.
- [20] W. Meinholt *et al.*, "A direct drive parallel plane piezoelectric needle positioning robot for MRI guided intraspinal injection," *IEEE Trans. Biomed. Eng.*, vol. 68, no. 3, pp. 807–814, Mar. 2021.
- [21] M. J. H. Lum *et al.*, "Teleoperation in surgical robotics-network latency effects on surgical performance," in *Proc. Annu. Int. Conf. IEEE Eng. Med. Biol. Soc.*, 2009, pp. 6860–6863.
- [22] S. Hutchinson *et al.*, "A tutorial on visual servo control," *IEEE Trans. Robot. Automat.*, vol. 12, no. 5, pp. 651–670, Oct. 1996.
- [23] M. Azizian *et al.*, "Visual servoing in medical robotics: A survey part i: Endoscopic and direct vision imaging-techniques and applications," *Int. J. Med. Robot. Comput. Assist. Surg.*, vol. 10, no. 3, pp. 263–274, 2014.
- [24] M. Azizian *et al.*, "Visual servoing in medical robotics: A survey part ii: Tomographic imaging modalities-techniques and applications," *Int. J. Med. Robot. Comput. Assist. Surg.*, vol. 11, no. 1, pp. 67–79, 2015.
- [25] D. H. Cortes *et al.*, "The shear modulus of the nucleus pulposus measured using magnetic resonance elastography: A potential biomarker for intervertebral disc degeneration," *Magn. Reson. Med.*, vol. 72, no. 1, pp. 211–219, 2014.
- [26] E. I. Ben-Abraham *et al.*, "Feasibility of mr elastography of the intervertebral disc," *Magn. Reson. Imag.*, vol. 39, pp. 132–137, 2017.
- [27] P. F. Beauchemin *et al.*, "Frequency-dependent shear properties of annulus fibrosus and nucleus pulposus by magnetic resonance elastography," *NMR Biomed.*, vol. 31, no. 10, 2018, Art. no. e3918.
- [28] A. Booeshaghi *et al.*, "Principles of open source bioinstrumentation applied to the poseidon syringe pump system," *Sci. Rep.*, vol. 9, no. 1, pp. 1–8, 2019.
- [29] K. Hosoda and M. Asada, "Versatile visual servoing without knowledge of true jacobian," in *Proc. IEEE/RSJ Int. Conf. Intell. Robots Syst.*, 1994, vol. 1, pp. 186–193.
- [30] T. E. Oliphant *et al.*, "Complex-valued stiffness reconstruction for magnetic resonance elastography by algebraic inversion of the differential equation," *Magn. Reson. Med.: An Official J. Int. Soc. Magn. Reson. Med.*, vol. 45, no. 2, pp. 299–310, 2001.
- [31] W. C. W. Chan *et al.*, "Structure and biology of the intervertebral disk in health and disease," *Orthopedic Clin.*, vol. 42, no. 4, pp. 447–464, 2011.
- [32] E. H. Clayton *et al.*, "Transmission, attenuation and reflection of shear waves in the human brain," *J. Roy. Soc. Interface*, vol. 9, no. 76, pp. 2899–2910, 2012.
- [33] W. Neumann *et al.*, "A novel 3D printed mechanical actuator using centrifugal force for magnetic resonance elastography: Initial results in an anthropomorphic prostate phantom," *PLoS One*, vol. 13, no. 10, 2018, Art. no. e0205442.